

# Structural, elastic and thermal properties of cementite ( $\text{Fe}_3\text{C}$ ) calculated using Modified Embedded Atom Method

Laalitha Liyanage

*Department of Physics and Astronomy, Mississippi State University, Mississippi State, MS 39762, USA and  
Center for Advanced Vehicular Systems, Mississippi State University, Mississippi State, MS 39762, USA*

Jeff Houze, Sungho Kim, and M. A. Tschopp

*Center for Advanced Vehicular Systems, Mississippi State University, Mississippi State, MS 39762, USA*

Seong-Gon Kim\*

*Department of Physics and Astronomy, Mississippi State University, Mississippi State, MS 39762, USA  
Center for Computational Science, Mississippi State University, Mississippi State, MS 39762, USA and  
Center for Advanced Vehicular Systems, Mississippi State University, Mississippi State, MS 39762, USA*

M. I. Baskes

*Department of Mechanical and Aerospace Engineering,  
University of California, San Diego, La Jolla, CA 92093, USA and  
Los Alamos National Laboratory Los Alamos, NM 87545, USA*

M. F. Horstemeyer

*Department of Mechanical Engineering, Mississippi State University, Mississippi State, MS 39762, USA and  
Center for Advanced Vehicular Systems, Mississippi State University, Mississippi State, MS 39762, USA*

(Dated: December 2, 2024)

Structural, elastic and thermal properties of cementite ( $\text{Fe}_3\text{C}$ ) were studied using a newly developed Modified Embedded Atom Method (MEAM) potential for the Fe-C alloy system. Previously developed Fe and C single element potentials were used to develop the Fe-C alloy potential. The single element potential for C correctly predicts both graphite and diamond as minimum energy structures. The alloy potential was developed using a statistically based optimization scheme to reproduce the heats of formation of element pairs in  $\text{L}_{12}$ ,  $\text{B}_1$  and cementite structures, and the interstitial energies of C in bcc Fe. The stability of cementite was investigated by molecular dynamics simulations at high temperatures. The nine single crystal elastic constants for cementite were obtained by computing total energies for strained cells. Polycrystalline elastic moduli for cementite were calculated from the single crystal elastic constants of cementite. Surface formation energies of (001), (010) and (100) surfaces of cementite were also calculated. The melting temperature and variation of specific heat and volume with respect to temperature, were investigated by performing a two-phase (solid/liquid) simulation of cementite. The predictions of the potential are in good agreement with first principles calculations and experiments.

PACS numbers: 61.50.Lt, 62.20.de, 61.72.jj, 71.15.Nc, 71.15.Pd

## I. INTRODUCTION

Steel alloys are the most widely used structural materials due to their abundance, all-purpose applicability and low cost. The main carbide in steel alloys is cementite which forms as a precipitate. Cementite has a direct impact on the mechanical, structural and thermal properties of steel. Therefore the ability to describe and predict the properties of cementite at the nanoscale is essential, in the study and design of new steels. Atomistic simulation methods, such as Molecular Dynamics or Monte Carlo simulations, offer an efficient and reliable route to investigate nanoscale mechanics pertaining to cementite in steel alloys. Each of these methods requires accurate interatomic potentials to find the energy of the system under investigation. First principles calculations, although the most reliable, are incapable of simulating the number of atoms required for realis-

tic calculations, due to unreasonable memory and time requirements. Here, semi-empirical potentials are being explored as a suitable alternative.

Among the spectrum of semi-empirical formulations, the Modified Embedded Atom Method (MEAM) has the ability to accurately predict properties of most crystal structures, such as bcc, fcc, hcp, and even diatomic, gases in good agreement with experiments or first principles calculations.<sup>1</sup> MEAM was proposed by Baskes et al.<sup>1</sup> and is a modification of the Embedded Atom Method (EAM)<sup>2</sup> that includes the directionality of bonds. In the original MEAM formalism, only first nearest neighbor interactions are considered.<sup>1</sup> Lee and Baskes<sup>3</sup> modified the original formalism to include screened second nearest neighbor (2NN) interactions. For further details of the MEAM formalism, we direct the reader to references 1 and 3.

The only existing 2NN MEAM potential for the iron-

carbon (Fe-C) system was developed by Byeong-joo Lee.<sup>4</sup> Lee's potential is designed to predict interactions of C interstitial atoms with defects such as vacancies. According to Fang et al.,<sup>5</sup> Lee's potential predicts a negative heat of formation for cementite. Lee's potential also predicts that cementite is only stable up to a temperature of 750 K.<sup>5</sup> Experimentally, however, cementite is metastable with a positive heat of formation.<sup>6</sup> Moreover, according to the iron-iron carbide phase diagram,<sup>7</sup> cementite is stable up to 1420 K. Among recent interatomic potentials<sup>8–12</sup> for the Fe-C system, EAM potentials by Lau et al.<sup>9</sup> and Ruda et al.<sup>11</sup> and the analytical bond order potential (ABOP) by Henriksson et al.<sup>12</sup> all promise to predict properties of cementite reasonably well. In the potentials by Lau et al.<sup>9</sup> and Ruda et al.,<sup>11</sup> however, the single element potential for C does not predict properties of both graphite and diamond well. This is due to the limited ability of EAM to describe the bare C-C interaction successfully.<sup>13</sup> We believe that a successful interatomic potential for an alloy system should not only predict the properties of the alloy correctly, but it should also predict the properties of the individual alloying elements in their natural crystal structures accurately. The ABOP by Henriksson et al.<sup>12</sup> predicts properties of cementite as well as Fe and C accurately, however ABOPs are not applicable to simulations involving interfaces and surfaces.<sup>14</sup> Also ABOPs are restricted to considering only first nearest neighbor interactions.<sup>14,15</sup> Most recent potentials for the Fe-C system are implemented using in-house developed molecular dynamics codes, which limits the potentials' transferability. We have used MEAM as implemented in the classical molecular dynamics simulation code LAMMPS<sup>16,17</sup> from Sandia National Laboratories for all atomistic simulations described in this paper.

In this study we develop a 2NN MEAM potential for the Fe-C alloy system that accurately predicts the structure and properties of cementite. Our alloy potential is based on previously developed 2NN MEAM potentials for pure Fe<sup>18</sup> and for pure C.<sup>19</sup> The C MEAM potential predicts both diamond and graphite as minimum energy structures with almost degenerate energies. Using the Fe and C single element potentials, the alloy potential for Fe-C was generated by fitting to the heats of formation of element pairs in the  $L_{12}$  and  $B_1$  crystal structures.  $Fe_3C$  in the  $L_{12}$  structure and  $FeC$  in the  $B_1$  structure are hypothetical crystal structures that do not exist in nature. Therefore properties of Fe-C in  $L_{12}$  and  $B_1$  crystal structures were obtained by first principles calculations. We performed first principles calculations using density functional theory (DFT)<sup>20,21</sup> and projector augmented wave (PAW) pseudopotentials.<sup>22</sup> Electron exchange and correlation were treated with generalized gradient approximation as parameterized by Perdew et al.<sup>23</sup> Brillouin zone sampling was performed using the Monkhorst-Pack scheme,<sup>24</sup> with a Fermi-level smearing of 0.2 eV applied through the Methfessel-Paxton method.<sup>25</sup> Geometric optimizations were carried out using conjugate gradient minimization method.<sup>20</sup> The constructed Fe-C al-

loy potential was optimized through a statistically based optimization scheme to reproduce heats of formation of element pairs in cementite, and interstitial energies of C in bcc Fe.

The paper is organized in the following manner. Section II describes the single-element interatomic potentials, their energy dependence on nearest neighbor distance, and predicted material properties compared to DFT and experimental data. Section II also includes the Fe-C MEAM alloy potential parameters and its predictions compared with Fe-C interatomic potentials published by Ruda et al.<sup>11</sup> and Henriksson et al.<sup>12</sup> Section III presents structural and elastic properties of cementite, as predicted by the Fe-C alloy potential and compared to DFT calculations, experimental values and interatomic potentials by Ruda et al.<sup>11</sup> and Henriksson et al.<sup>12</sup> In section IV, thermal properties of cementite, such as melting temperature and variation of specific heat and volume with respect to temperature, are investigated.

## II. MEAM POTENTIALS

### A. Single element potentials

The single element MEAM potential parameters are presented in Table I. The parameters for Fe are from the MEAM potential developed by Lee et al.<sup>18</sup> and the parameters for C are from Uddin et al.<sup>19</sup>

#### 1. Energy vs. nearest neighbor distance curves

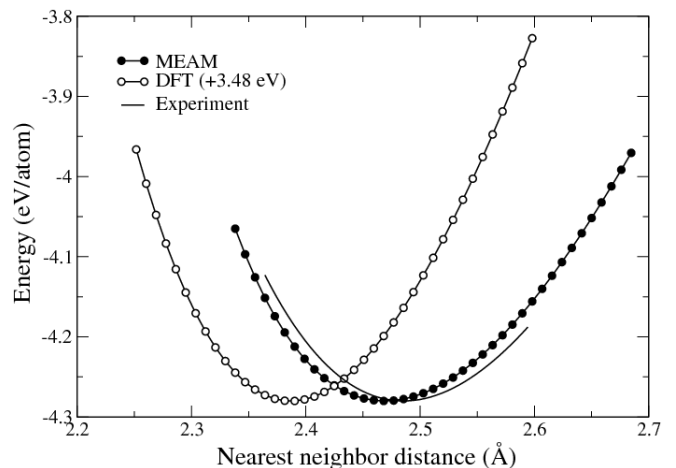


FIG. 1. Comparison of energy vs. nearest neighbor distance curves for Fe. The solid curve is constructed from experimental values in Table II. For comparison, the DFT curve is shifted vertically to the experimental cohesive energy of Fe at the equilibrium nearest neighbor distance.

Energy vs. nearest neighbor distance curves are considered important tests of validity for interatomic poten-

TABLE I. MEAM potential parameters for Fe, C and Fe-C. The parameters include, the reference structure ‘lattice,’ heat of formation of reference structure  $\Delta$ , equilibrium nearest neighbor distance of the reference structure  $r_e$ , exponential decay factor for the universal energy  $\alpha$ , additional cubic term in the universal energy equation  $a_3$ , cohesive energy  $E_c$ , embedding energy scaling factor  $A$ , atomic density exponential decay factors  $\beta^{(0-3)}$ , weighting factors for atomic densities  $t^{(0-3)}$ , density scaling factor  $\rho_0$ , cutoff radius  $r_{\text{cut}}$ , and angular screening parameters  $C_{\text{max}}$  and  $C_{\text{min}}$  ( $i - j - k$  represents  $k$  atom in between  $i$  and  $j$  atoms). Alternative averaging of densities was used for the alloy (ialloy = 1).<sup>17</sup>

MEAM potentials				Angular screening parameters		
Property	Fe	C	Fe-C	$i - j - k$	$C_{\text{max}}$	$C_{\text{min}}$
lattice	bcc	diamond	$B_1$	Fe-Fe-Fe	1.9	0.68
$\Delta$ (eV/atom)			0.002	Fe-Fe-C	2.8	0.06
$r_e$ (Å)	2.469	1.545	1.92	Fe-C-Fe	2.8	2.0
$\alpha$	5.027	4.38	4.75	Fe-C-C	2.8	2.0
$a_3$	0.3	0.0	0.125	C-C-Fe	2.8	0.5
$E_c$ (eV/atom)	4.28	7.37		C-C-C	2.8	2.0
$A$	0.585	1.49				
$\beta^{(0)}$	3.8	4.26				
$\beta^{(1)}$	2.0	5.0				
$\beta^{(2)}$	0.9	3.2				
$\beta^{(3)}$	0.0	3.98				
$t^{(0)}$	1.0	1.0				
$t^{(1)}$	-0.8	7.5				
$t^{(2)}$	12.3	1.04				
$t^{(3)}$	2.0	-1.01				
$\rho_0$	1.0	5.49				
$r_{\text{cut}}$ (Å)	4.5	4.5	4.5			

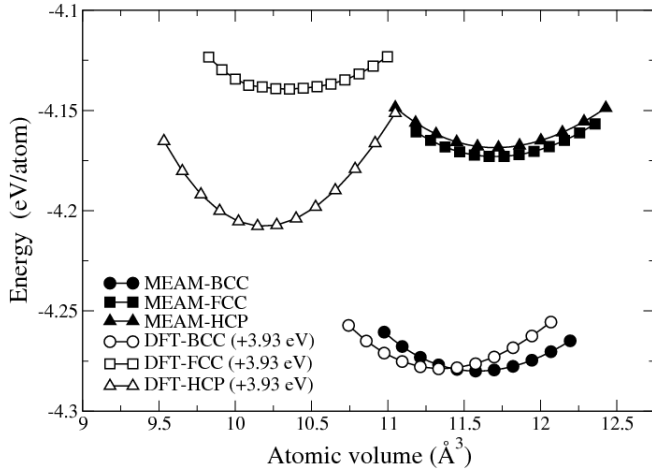


FIG. 2. Comparison of energy vs. volume curves for Fe in bcc, fcc and hcp crystal structures. For ease of comparison, the DFT curves are shifted vertically by a constant value, equal to the difference between experimental and DFT cohesive energies of Fe in bcc at equilibrium volumes.

tials. Here we present the energy vs. nearest neighbor distance curves generated by the single element potentials for Fe and C. Fig. 1 shows the comparison of energy vs. nearest neighbor distance curve for bcc Fe, compared to the curves generated by DFT calculations and

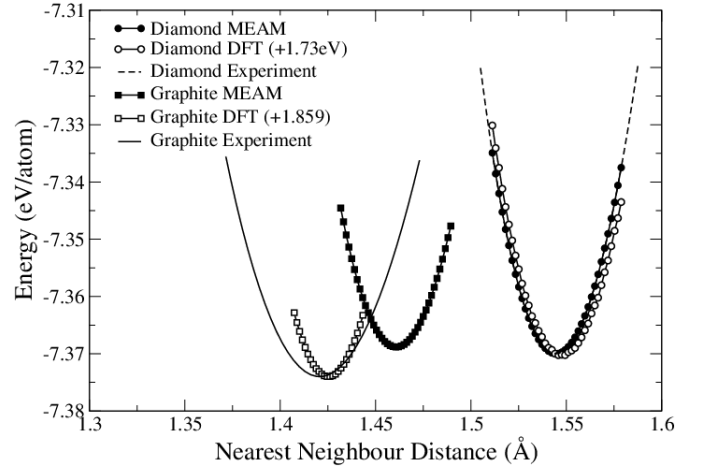


FIG. 3. Comparison of energy vs. nearest neighbor distance curves for C in diamond and graphite structures. The solid curve is constructed from experimental values in Table II. For comparison, the DFT curve is shifted vertically to the experimental cohesive energy at the equilibrium nearest neighbor distance.

experimental data. It is well known that DFT overestimates the cohesive energy.<sup>26</sup> Therefore the DFT curve is shifted to the experimental cohesive energy at the equilibrium nearest neighbor distance to ease comparison of

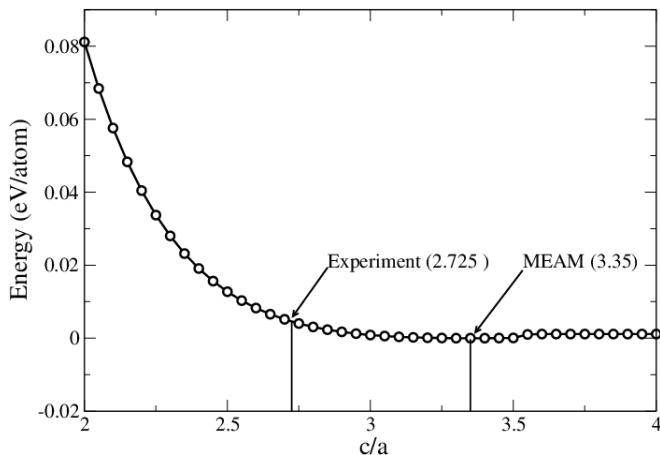


FIG. 4. Cohesive energy of graphite as a function of the  $c/a$  ratio. Energy at zero is set to the minimum energy predicted by MEAM.

curves. Due to overbinding, DFT prediction for equilibrium nearest neighbor distance is underestimated.<sup>27</sup> Therefore the DFT curve sits to the left of the experimental curve. The experimental curve was constructed from the Rose's equation of state<sup>28</sup> using the experimental bulk modulus, cohesive energy and nearest neighbor distance, listed in Table II. As shown in Fig 2, the stability of Fe in the bcc structure was compared to that of Fe in the fcc and hcp structures. Fe in the bcc is the most stable of these structures, as predicted by the Fe MEAM potential. MEAM predicts that fcc and hcp Fe are much closer in energy and have a significantly larger volume than that calculated from DFT.

C single element MEAM potential predicts diamond and graphite both to be stable structures. Energy vs. nearest neighbor distance curves, for diamond and graphite are shown in Fig. 3. MEAM predictions for diamond and graphite has good agreement with experimental results. MEAM predicts almost degenerate energies for graphite and diamond, while DFT predicts graphite to be  $\sim 0.1$  eV more stable than diamond. For graphite, DFT predicts a first nearest neighbor (1NN) distance in good agreement with experimental data, while MEAM predicts a 1NN distance  $\sim 3\%$  greater than the experimental values. MEAM optimized the  $c/a$  ratio of the graphite structure to 3.35. This does not agree with the experimental value of 2.725.<sup>29</sup> The disagreement is due to the incorrect prediction of interlayer interactions of graphite, which are dominated by van Der Waals forces, that are not described by MEAM. However the dependence of cohesive energy on the  $c/a$  ratio is small. As illustrated in Fig. 4, the difference in cohesive energy of graphite between the experimental and MEAM  $c/a$  ratio is  $\sim 4$  meV/atom. In constructing the energy vs. nearest neighbor distance curves for graphite, the inter-planar distance was scaled with the lattice constant. The experimental ratio was used in the generation of the DFT curve, while the MEAM curve was constructed with the

predicted  $c/a$  ratio.

## 2. Single element material properties

Cohesive energy, equilibrium lattice constant and bulk modulus for bcc Fe, graphite and diamond were determined through fitting the Murnaghan's equation of state<sup>30,31</sup> to the energy vs. volume curves generated by MEAM. The single element material properties compared to experimental values are shown in Table II.

TABLE II. Material properties predicted by the single element MEAM potentials.  $E_c$  is the Cohesive Energy,  $a$  and  $c$  are the equilibrium lattice constants, and  $B$  is the bulk modulus. Experimental values are given in parentheses.

Property	bcc Fe	diamond	graphite
$E_c$ (eV/atom)	-4.29 (-4.28) <sup>a</sup>	-7.37 (-7.37) <sup>c</sup>	-7.369 (-7.374) <sup>d</sup>
$B$ (GPa)	177 (168) <sup>b</sup>	443 (443) <sup>c</sup>	176 (286) <sup>d</sup>
$a$ (Å)	2.85 (2.86) <sup>b</sup>	3.57 (3.567) <sup>c</sup>	2.53 (2.461) <sup>d</sup>
$c$ (Å)			8.476 (6.709) <sup>d</sup>

<sup>a</sup> Philipson et al.<sup>26</sup>

<sup>b</sup> Wang et al.<sup>32</sup>

<sup>c</sup> References 33–35 as reported by Fahy et al.<sup>36</sup>

<sup>d</sup> References 30, 35, and 37 as reported by Yin et al.<sup>29</sup>

## B. MEAM potential for Fe-C alloy

The MEAM potential parameters for the Fe-C alloy potential were fit to the heats of formation of  $B_1$ ,  $L_{12}$  and cementite ( $Fe_3C$ ), and interstitial energies of C in bcc Fe. First principle calculations were performed to determine heats of formation of Fe-C alloy in  $B_1$ ,  $L_{12}$  and cementite ( $Fe_3C$ ) structures, and interstitial energies of C in bcc Fe lattice at octahedral and tetrahedral positions. The potential was fitted to target values through a statistically-based optimization scheme developed by Tschoopp et al.<sup>38</sup> This scheme uses a stratified random sampling approach (Latin Hypercube Sampling<sup>39</sup>(LHS)) to sample the  $N$ -parameter space, with  $N$  being the number of potential parameters sensitive to the targets considered. A sensitivity analysis was completed at the beginning of the optimization to determine parameters of the potential model most sensitive to the targets. Next, random sampling of the parameter space was done using LHS, with 4000 different potential parameter combinations. Then analytical models were generated to provide a representation of the correlation between potential parameters and target values. Once the models were generated, a multi-objective optimization was executed to determine the best possible values for the parameters. Considerable efforts were made to match the order of stability of the two C interstitial energies in bcc Fe and the heats of

formation of  $B_1$ ,  $L_{12}$  and cementite structures. The final parameters of the alloy potential are presented in Table I. Table III lists the MEAM prediction of the target properties used for fitting of the potential, compared with either DFT or experimental values and with interatomic potentials by Ruda et al.<sup>11</sup> and Henriksson et al.<sup>12</sup> The order of stability of  $B_1$ ,  $L_{12}$  and cementite structures are predicted correctly compared with DFT results. MEAM predicts the heats of formation of  $B_1$  and  $L_{12}$  structures in good agreement with DFT. MEAM prediction of the heat of formation of cementite is in excellent agreement with DFT and experimental data. Predicted interstitial energies of C in tetrahedral and octahedral positions of bcc Fe have the same order of magnitude as DFT. As in DFT, MEAM predicts the octahedral interstitial to be more stable than the tetrahedral interstitial. However, neither MEAM or literature potentials predict the energy difference between the two interstitials as in DFT.

### 1. Energy vs. nearest neighbor distance curves for $B_1$ and $L_{12}$ structures.

The cohesive energy of Fe-C in the  $B_1$  and  $L_{12}$  crystal structures as a function of the nearest neighbor distance is shown in Figs. 5 and 6, respectively. For the  $B_1$  structure, MEAM predicts a lattice constant 4% less and a bulk modulus 0.3% less than the DFT results. MEAM prediction for the  $L_{12}$  structure gives a lattice constant 3.4% greater and a bulk modulus 35% less than DFT predicts. As mentioned earlier, DFT overestimates the cohesive energy. Therefore the DFT curve is shifted vertically in these figures to ease comparison with the MEAM curve.

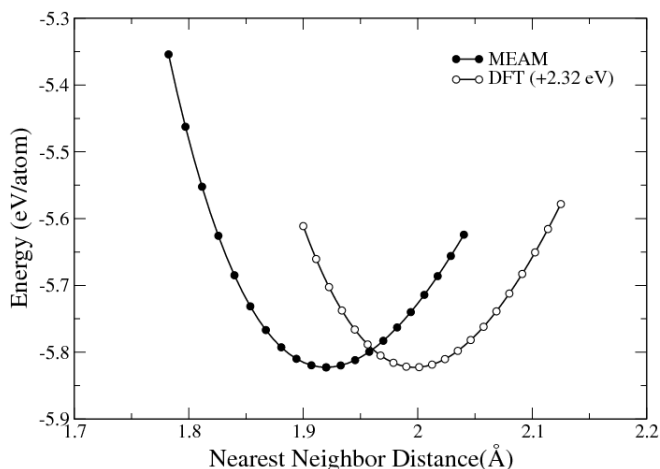


FIG. 5. Comparison of energy vs. nearest neighbour distance curves of Fe-C alloy system in  $B_1$  structure. DFT curve is shifted vertically for comparison with the MEAM curve.

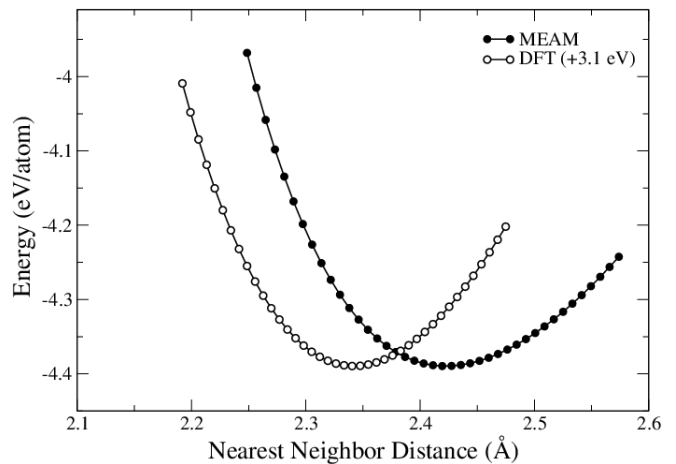


FIG. 6. Comparison of energy vs. nearest neighbour distance curves of Fe-C alloy system in  $L_{12}$  structure. DFT curve is shifted vertically for comparison with the MEAM curve.

### 2. Elastic constants of FeC in the $B_1$ crystal structure

Elastic constants of Fe-C in the  $B_1$  crystal structure were calculated using the Fe-C MEAM potential. They are presented in Table IV in comparison with DFT calculations. They were calculated using the deformation matrix presented in Jiang et al.<sup>40</sup> In linear elastic theory, deformation energy is a function of strain. Distortion energies ( $\Delta E$ ) calculated for strains ( $\delta$ ) equal to  $\pm 2\%$  and  $\pm 0.1\%$  were fitted to  $\Delta E = k_2\delta^2 + k_3\delta$ . DFT calculations were only performed for  $\delta = \pm 2\%$ . The single-crystal elastic constants were obtained using the relationships for the quadratic coefficient  $k_2$  listed in Jiang et al.<sup>40</sup> Current results for  $c_{11}$  agree with DFT results.  $c_{12}$  is predicted at a lower value than DFT predictions, but it is in the same order of magnitude. MEAM prediction of  $c_{44}$  is significantly larger than DFT.

## III. STRUCTURAL AND ELASTIC PROPERTIES OF CEMENTITE.

Structural properties of cementite were calculated, including equilibrium lattice parameters, equilibrium volume, and heat of formation. These properties are presented in Table V with comparison to DFT calculations, experimental data and to interatomic potentials by Ruda et al.<sup>11</sup> and Henriksson et al.<sup>12</sup> As noted in Section II B MEAM prediction of the heat of formation of cementite has excellent agreement with DFT and experimental data. Henriksson's potential also predicts a value in good agreement with DFT and experimental values, while Ruda's potential predicts a much larger value. Lattice constants of MEAM and literature potentials<sup>11,12</sup> agree well with experimental results, while DFT predicts lower values. As a test of validity, the variation of cohesive energy with volume was calculated. Fig. 7 compares

TABLE III. Material properties of Fe and C in  $B_1$ ,  $L_{12}$  and cementite structures and interstitial energies of C in Fe, used for potential generation.  $\Delta H_f$  is the heat of formation. Experimental data are in parenthesis.

Property	DFT	This work	Ruda <sup>11</sup>	Henriksson <sup>12</sup>
$B_1$ $\Delta H_f$ (eV/atom)	0.29	0.17		
$L_{12}$ $\Delta H_f$ (eV/atom)	0.36	0.45		
Cementite $\Delta H_f$ (eV/atom)	0.01(0.05) <sup>a</sup>	0.06	0.18	0.03
C interstitial energies in bcc Fe (eV)				
Tetrahedral	2.14	1.74	2.08	1.50
Octahedral	1.25	1.55	1.81	1.18

<sup>a</sup> Meschel et al.<sup>6</sup>

TABLE IV. Elastic moduli (GPa) of FeC in the  $B_1$  structure.

Property	DFT $\delta = \pm 2\%$	This work $\delta = \pm 2\%$	This work $\delta = \pm 0.1\%$
$c_{11}$	601	570	566
$c_{12}$	589	213	213
$c_{44}$	83	391	389

the energy vs. volume curves for cementite generated by our MEAM potential with DFT and experimental curves. During volume variation of cementite, the ratios between  $a, b$  and  $c$  lattice parameters were held constant. As noted before, DFT overestimates the cohesive energy and underestimates the volume. Therefore the DFT curve is to the left of the experimental curve. For ease of comparison the DFT curve is shifted vertically to the experimental cohesive energy at equilibrium volume. The experimental curve was generated by Murnaghan's equation of state<sup>30,31</sup> with the experimental bulk modulus, volume and cohesive energy.<sup>41</sup> Experimentally single-crystal bulk modulus of cementite has not been determined. Therefore the polycrystalline bulk modulus of cementite was used to generate the experimental curve.

#### A. Single-crystal elastic properties

The elastic moduli of cementite were calculated, then compared to DFT calculations and to interatomic potentials by Ruda et al.<sup>11</sup> and Henriksson et al.<sup>12</sup> They were calculated using the deformation matrices described in Jiang et al.<sup>40</sup> We fitted distortion energies ( $\Delta E$ ) calculated for strains  $\pm\delta$  to the function  $\Delta E = k_2\delta^2 + k_3\delta$  and used the relationships for the quadratic coefficient  $k_2$  outlined in Jiang et al.<sup>40</sup>  $\delta = 0.5\%$  and  $\delta = 0.1\%$  were used to compare the results to the DFT values calculated at the same strains. Results for both strain values produced the same results. As presented in Table VI, the MEAM predictions for elastic constants are positive but have considerable disagreement with DFT values. However, MEAM and literature potentials could not reproduce the low value of  $c_{44}$  reported by DFT.<sup>40</sup> Percentage differences from the DFT predictions are indicated in the

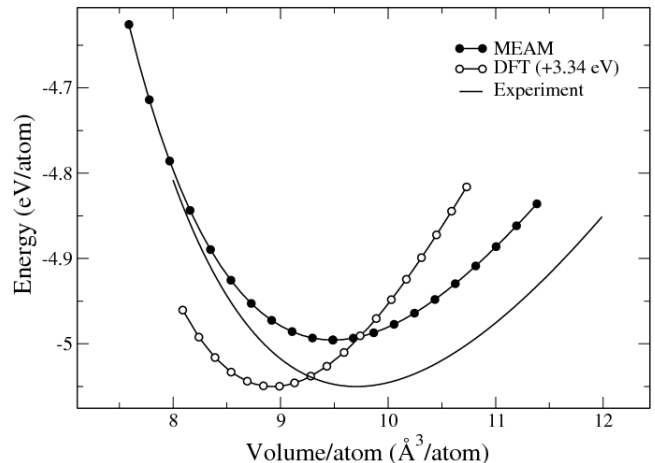


FIG. 7. Comparison of energy vs. volume curves for cementite. The solid curve is constructed from experimental values of the cohesive energy, polycrystalline bulk modulus, and equilibrium volume of cementite. For comparison, the DFT curve is shifted vertically to the experimental cohesive energy at equilibrium volume.

table for ease of comparison.

#### B. Polycrystalline elastic properties

Theoretical upper and lower bounds for the polycrystalline bulk modulus ( $B$ ) and shear modulus ( $G$ ) were calculated using the single-crystal elastic constants according to methods by Reuss and Voigt.<sup>40,43</sup> The true polycrystalline  $B$  and  $G$  were then estimated using Hill's average.<sup>40,44</sup> Young's modulus ( $Y$ ) and Poisson's ratio ( $\nu$ ) were calculated by using equations 1 and 2.<sup>40</sup>

$$Y = 9BG/(3B + G) \quad (1)$$

$$\nu = (3B/2 - G)/(3B + G) \quad (2)$$

Polycrystalline elastic moduli predicted by our MEAM potential are presented in Table VII, in comparison with DFT calculations, experimental results, and interatomic potentials by Ruda et al.<sup>11</sup> and Henriksson et al.<sup>12</sup> The

TABLE V. Material properties of cementite.  $\Delta H_f$  is heat of formation,  $\Omega_0$  is the equilibrium volume,  $a$ ,  $b$  and  $c$  are the lattice parameters. Experimental data are in parentheses.

Property	DFT	This work	Ruda <sup>11</sup>	Henriksson <sup>12</sup>
$\Delta H_f$ (eV/atom)	0.01 (0.05) <sup>a</sup>	0.06	0.18	0.03
$\Omega_0$ ( $\text{\AA}^3/\text{atom}$ )	8.49 (9.71) <sup>b</sup>	9.49	9.11	9.33
$a$ ( $\text{\AA}$ )	4.91 (5.09) <sup>b</sup>	5.05	5.14	5.09
$b$ ( $\text{\AA}$ )	6.63 (6.74) <sup>b</sup>	6.69	6.52	6.52
$c$ ( $\text{\AA}$ )	4.38 (4.53) <sup>b</sup>	4.49	4.35	4.50

<sup>a</sup> Meschel et al.<sup>6</sup>

<sup>b</sup> Umemoto et al.<sup>42</sup>

TABLE VI. Single-crystal elastic moduli,  $C_{xy}$ (GPa) of cementite. Percentage difference from DFT predictions are given in parentheses.

Property	DFT <sup>40</sup>	This work		Ruda <sup>11</sup>		Henriksson <sup>12</sup>	
$c_{11}$	395	303	(−23%)	263	(−33%)	363	(−8%)
$c_{22}$	347	216	(−38%)	219	(−37%)	406	(17%)
$c_{33}$	325	307	(−6%)	247	(−24%)	388	(19%)
$c_{12}$	158	126	(−20%)	176	(11%)	181	(15%)
$c_{23}$	163	110	(−33%)	143	(−12%)	130	(−20%)
$c_{13}$	169	157	(−7%)	146	(−14%)	166	(−2%)
$c_{44}$	18	249	(1283%)	77	(328%)	91	(406%)
$c_{55}$	134	236	(76%)	95	(−29%)	125	(−7%)
$c_{66}$	135	227	(68%)	123	(−9%)	134	(−1%)

elastic constants predicted by DFT are in excellent agreement with experimental data. MEAM predicts the best agreement of the potentials with experimental value for B; however, the MEAM prediction of  $\nu$  is significantly lower than its experimental value. Ruda’s potential predicts the best agreement with experimental results for G and  $\nu$ .

### C. Surface energies

$$E_{\text{surf}} = (E_{\text{slab}} - N\varepsilon)/A \quad (3)$$

Calculations were performed on (001), (010), and (100) surfaces to determine the surface formation energy. The surface formation energy per unit area is defined as in equation 3.  $E_{\text{slab}}$  is the energy of the system with a surface consisting of  $N$  atoms,  $\varepsilon$  is the energy per atom in the bulk system, and  $A$  is the surface area. Table VIII compares the surface formation energies of this work to DFT calculations and to the interatomic potential by Ruda et al.<sup>11</sup> The predicted surface energies have the same order of magnitude as DFT results. However, MEAM is unsuccessful in predicting the surface anisotropy predicted by DFT calculations.

## IV. THERMAL PROPERTIES OF CEMENTITE

The stability of cementite at high temperatures was investigated through molecular dynamics (MD) simulations in the canonical (NVT) ensemble at 300 K and 800 K. At the end of these MD simulations, cementite retained its crystalline structure, affirming its stability at high temperatures. The newly developed Fe-C MEAM potential was used to predict several thermal properties of cementite. In this section we present calculations for predicting melting temperature and variation of specific heat and volume of cementite with respect to temperature.

### A. Melting temperature

The melting temperature of cementite is not well defined due to its instability at high temperatures. The Fe-C phase diagram indicates a eutectic point at 1420 K,<sup>7</sup> where liquid consisting of Fe and C solidifies to form austenite and cementite crystals. For the purpose of this calculation, we considered the melting temperature of cementite to be the temperature when cementite loses its crystal structure and becomes a random collection of Fe and C atoms similar to the eutectic point. Conventionally, melting temperature calculations are done using a single-phase simulation box. The single phase method generally overestimates the melting temperature. The overestimation is a result of the exclusion of interface effects.<sup>49</sup> By using a two-phase simulation box, a box

TABLE VII. Comparison of polycrystalline cementite properties, bulk modulus (B), shear modulus (G), Young's modulus (Y) and Poisson's ratio ( $\nu$ ).

Property	DFT <sup>40</sup>	Experimental	This work	Ruda <sup>11</sup>	Henriksson <sup>12</sup>
$B$ (GPa)	224	$175 \pm 4$ <sup>a</sup>	174	183	234
$G$ (GPa)	72	74 <sup>b</sup>	146	69	114
$Y$ (GPa)	194	$177$ <sup>c</sup> , $196$ <sup>d</sup> , $200$ <sup>b</sup>	343	184	293
$\nu$	0.36	0.36 <sup>b</sup>	0.17	0.33	0.29

<sup>a</sup> Scott et al.<sup>45</sup>

<sup>b</sup> Laszlo et al.<sup>46</sup>

<sup>c</sup> Mizubayashi et al.<sup>47</sup>

<sup>d</sup> Umemoto et al.<sup>42</sup>

TABLE VIII. Relaxed surface energies of cementite in  $J/m^2$

Surface	DFT <sup>48</sup>	This work	Ruda et al. <sup>11</sup>
(001)	2.05	2.30	1.96
(010)	2.26	1.81	2.00
(100)	2.47	1.79	2.34

that has a solid and a liquid phases, the melting temperature can be predicted more accurately.

### 1. Two-phase simulation (TPS)

We performed two-phase simulations (TPS) in the NPT ensemble to determine the melting temperature of cementite. The simulation box contained both solid and liquid phases of cementite. First, a supercell containing  $14 \times 7 \times 7$  unit cells of cementite (10976 atoms) was heated through MD runs in the NPT ensemble with  $T = 1200$  K and  $P = 0$ . Second, half of the atoms in the supercell were frozen, and MD runs were carried out in the NPT ensemble with  $T = 4000$  K and  $P = 0$ . The resulting supercell was then subjected to MD runs in the NPT ensemble with  $T = 1500$  K and  $P = 0$ , still keeping the same half of atoms frozen. The result of this process was a supercell containing solid cementite at 1200 K in one half and liquid cementite at 1500 K in the other half. This ensures minimum difference of stress between atoms in liquid and solid phases of the supercell. This supercell was then used in simulations of solidification and melting of cementite.

The two-phase supercell was heated through MD runs in the NPT ensemble where  $T$  ranged from 1000 K to 1600 K in 100 K intervals. Each system ran for 1.6 nanoseconds. The phase change of the two-phase simulation box was visually observed. At 1400 K the solid phase of the simulation box was progressing to occupy the entire box, and at 1500 K the liquid phase of the simulation box was progressing to occupy the entire box. Next the initial two-phase simulation box was heated from 1400 K to 1500 K in 10 K intervals using NPT molecular dynamic runs. Each system was equilibrated for at least 5 million time steps, where each time step was 2 fs, to-

taling to 10 ns. The final state of the system was visually inspected. If the final state appeared to have both liquid and solid phases, more MD runs were performed until the final state of the supercell contained one phase. Some systems required as much as 32 ns of MD runs to arrive at a single phase. The transformation of the two-phase simulation box to a one-phase simulation box near the predicted melting temperature is presented in Figs. 8 and 9. The total energy, volume, and pressure of the systems were determined through averaging the values of the final 40000 time steps (80 ps) of each simulation. The variation of properties such as total energy, volume, specific heat, and derivative of volume with temperature allows us to clearly determine the melting temperature of cementite. Plots illustrating these variations are presented in Fig. 10. Experimental data for heat capacity and volume are not available for the 1400 - 1500 K temperature range. Available experimental data are heat capacity at 1023 K  $3.6 k_B/\text{atom}$ ,<sup>50</sup> which converts to 3.4 eV/K for the current simulation, and experimental volume at 1070 K measured at  $10 \text{ \AA}^3/\text{atom}$ .<sup>51</sup> Specific heat and volume determined from first principle calculations<sup>52</sup> done on the solid phase of cementite are included for comparison in Fig. 10 plots (b) and (c). According to the plots of Fig. 10, we obtained a melting temperature between 1420 K and 1430 K. This is in good agreement with the experimental eutectic point at 1420 K.<sup>7</sup>

## V. CONCLUSION

We studied the properties of cementite using an interatomic potential developed in the MEAM formalism. Previously developed single element interatomic potentials for Fe and C were used for the development of the Fe-C alloy MEAM potential. The single element potential for C predicts graphite and diamond as minimum energy structures with almost degenerate energies. MEAM potentials for pure elements predict the heats of formation, bulk moduli and lattice constants of Fe and C in their natural crystal structures in good agreement with experimental data. The alloy potential for Fe-C system was developed to reproduce heats of formation of Fe and C in  $B_1$ ,  $L_{12}$ , and cementite ( $\text{Fe}_3\text{C}$ ) crystal structures



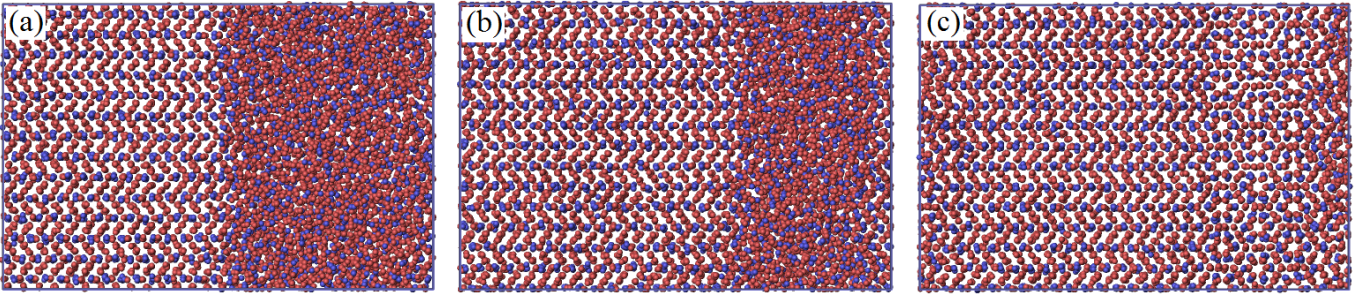


FIG. 8. (Color online) Snapshots of the two-phase MD simulation in the NPT ensemble with  $T = 1420$  K and  $P = 0$ . Red spheres are Fe atoms and blue spheres are C atoms. (a) Initial state of the simulation box, which contains both liquid and solid phases of cementite. (b) Intermediate state of the simulation box at 16 ns, as the solid phase propagates. (c) Final state of the simulation box at 32 ns, when the entire system has turned into the solid phase.

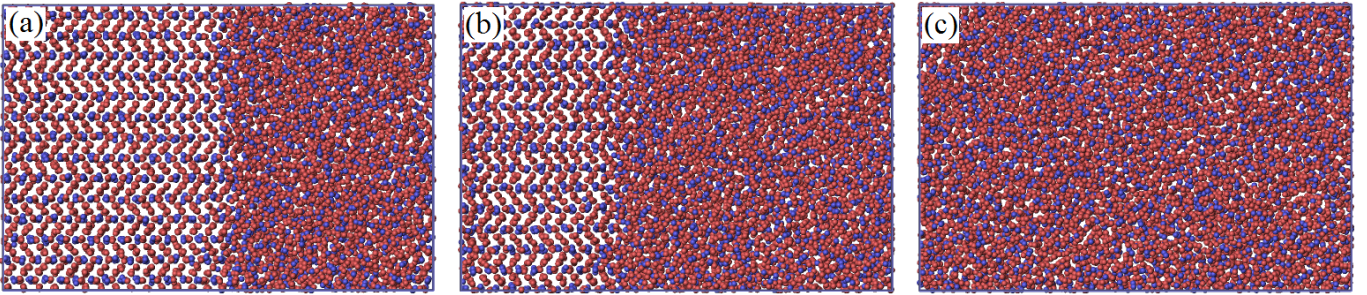


FIG. 9. (Color online) Snapshots of the two-phase MD simulation in the NPT ensemble with  $T = 1430$  K and  $P = 0$ . Red spheres are Fe atoms and blue spheres are C atoms. (a) Initial state of the simulation box, which contains both liquid and solid phases of cementite. (b) Intermediate state of the simulation box at 20 ns, as the liquid phase propagates. (c) Final state of the simulation box at 30 ns, when the entire system has turned into the liquid phase.

and interstitial energies of C in bcc Fe. The Fe-C potential was validated by investigation of energy variation with respect to nearest neighbor distance of Fe and C in  $B_1$  and  $L_{12}$  structures. The validated potential was used to predict structural, elastic and thermal properties of cementite. Structural properties included heat of formation, equilibrium lattice constants, equilibrium volume and the energy variation with respect to volume. MEAM predictions are in good agreement with DFT/experimental data. The nine single crystal elastic constants were calculated and used to estimate polycrystalline bulk modulus (B), shear modulus (G), Young's modulus (Y) and Poisson's ratio ( $\nu$ ) of cementite. MEAM predictions of the single-crystal elastic constants are positive but have considerable deviation from DFT results. Compared to literature potentials,<sup>11,12</sup> MEAM prediction of B agrees best with experimental values. Surface energies for (001), (010) and (100) surfaces were calculated as well. MEAM was not successful in predicting the surface anisotropy of cementite. Melting temperature and variation of specific heat and volume with respect to temperature was predicted by two-phase (solid/liquid) MD simulations. MEAM predicted the melting temperature to be between 1420 K and 1430 K. This is in good agreement to the eutectic point at 1420 K indicated in the Fe-C phase diagram.<sup>7</sup> Even though the potential was

fitted for ground state properties, its accuracy in predicting thermal properties of cementite at high temperatures proves its predictive capability. Therefore the potential can be used reliably to investigate the role of cementite in multi-component steel alloys.

## VI. ACKNOWLEDGMENTS

We are grateful to A.B. Belonoshko for his suggestions in conducting the two-phase melting simulations. This work was supported in part by the Department of Energy, grants DE-EE0002323 and DE-FC26-06NT2755.

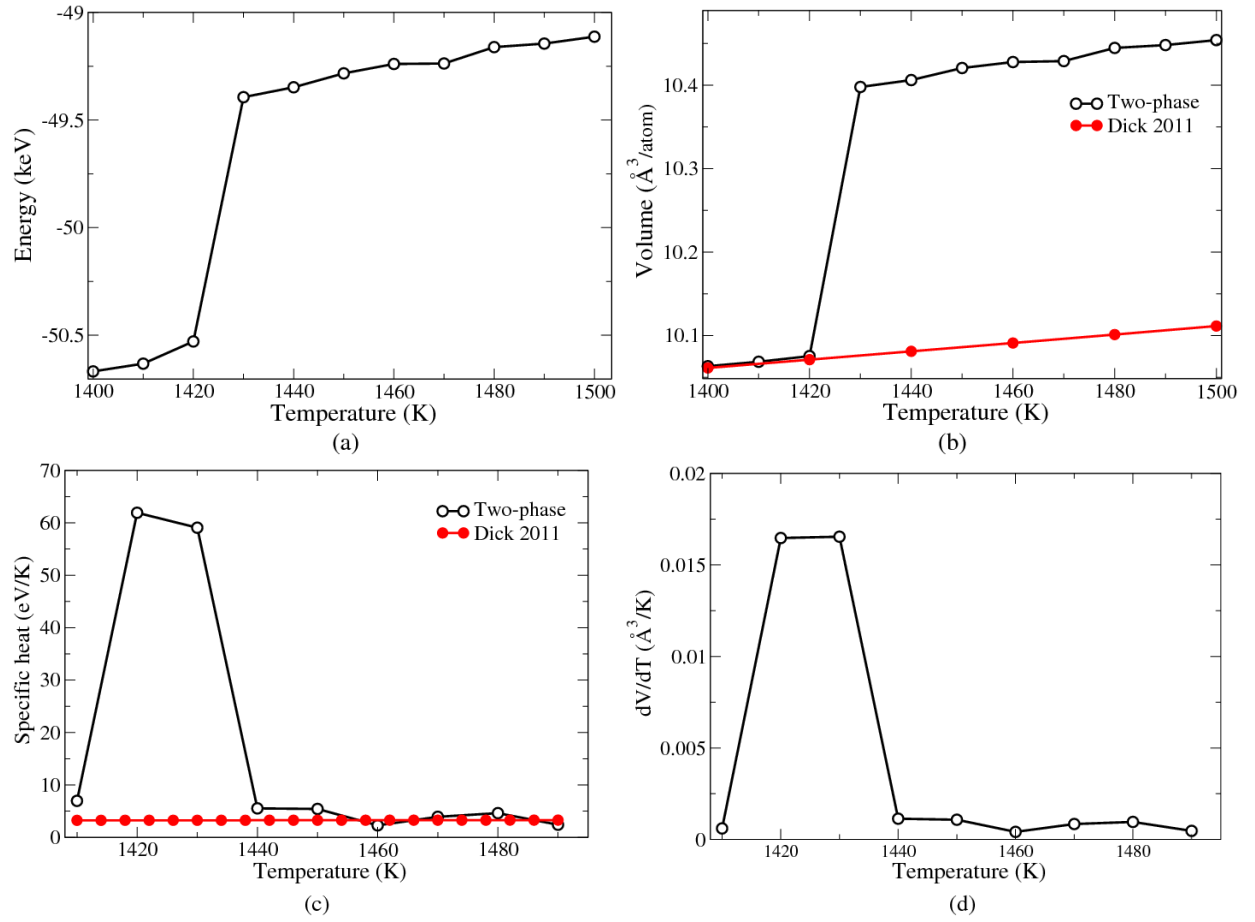


FIG. 10. Variation of properties of the two-phase system over temperature. (a) Total energy of the system. (b) (Color online) Volume of the system. Red curve is first principles data. (c) (Color online) Specific heat of the system. Red curve is first principles data. (d)  $dV/dT$  of the system.

- 
- \* Author to whom correspondence should be addressed; kimsg@hpc.msstate.edu
- <sup>1</sup> M. Baskes, Physical Review B **46**, 2727 (1992).
  - <sup>2</sup> M. S. Daw and M. I. Baskes, Phys. Rev. B **29**, 6443 (1984).
  - <sup>3</sup> B.-J. Lee, M. Baskes, H. Kim, and Y. Koo Cho, Physical Review B **64** (2001), 10.1103/PhysRevB.64.184102.
  - <sup>4</sup> B. Lee, Acta Materialia **54**, 701 (2006).
  - <sup>5</sup> C. F. Fang, M. A. v. Huis, B. J. Thijssen, and H. W. Zandbergen, Phys. Rev. B (2012).
  - <sup>6</sup> S. Meschel and O. Kleppa, Journal of Alloys and Compounds **257**, 227 (1997).
  - <sup>7</sup> W. Callister and D. Rethwisch, *Materials science and engineering: an introduction*, 7th ed. (Wiley New York, 2007) pp. 290–293.
  - <sup>8</sup> C. Becquart, J. Raulot, G. Bencteux, C. Domain, M. Perez, S. Garruchet, and H. Nguyen, Computational Materials Science **40**, 119 (2007).
  - <sup>9</sup> T. T. Lau, C. J. Först, X. Lin, J. D. Gale, S. Yip, and K. J. V. Vliet, Phys. Rev. Lett. **98**, 215501 (2007).
  - <sup>10</sup> D. Hepburn and G. Ackland, Physical Review B **78**, 1 (2008).
  - <sup>11</sup> M. Ruda, D. Farkas, and G. Garcia, Computational Materials Science **45**, 550 (2009).
  - <sup>12</sup> K. Henriksson and K. Nordlund, Physical Review B **79**, 1 (2009).
  - <sup>13</sup> A. Duff and M. Sluiter, Materials Transactions **51**, 675 (2010).
  - <sup>14</sup> P. Erhart, N. Juslin, O. Goy, K. Nordlund, R. Müller, and K. Albe, Journal of Physics: Condensed Matter **18**, 6585 (2006).
  - <sup>15</sup> K. Albe, K. Nordlund, and R. S. Averback, Phys. Rev. B **65**, 195124 (2002).
  - <sup>16</sup> Steve and Plimpton, Journal of Computational Physics **117**, 1 (1995).
  - <sup>17</sup> S. Plimpton, “Lammps-large-scale atomic/molecular massively parallel simulator,” April 2011 version, <http://lammps.sandia.gov/>.
  - <sup>18</sup> T. Lee, M. I. Baskes, S. M. Valone, and J. D. Doll, Los Alamos Preprint:LA-UR 11-03286 (2011).
  - <sup>19</sup> J. Uddin, M. I. Baskes, S. G. Srinivasan, T. R. Cundari, and A. K. Wilson, Phys. Rev. B **81**, 104103 (2010).
  - <sup>20</sup> G. Kresse and J. Hafner, Phys. Rev. B **47**, 558 (1993).

- <sup>21</sup> G. Kresse and J. Furthmüller, Physical Review B **54**, 11169 (1996).
- <sup>22</sup> G. Kresse and D. Joubert, Phys. Rev. B **59**, 1758 (1999).
- <sup>23</sup> J. P. Perdew, J. A. Chevary, S. H. Vosko, K. A. Jackson, M. R. Pederson, D. J. Singh, and C. Fiolhais, Physical Review B **46**, 6671 (1992).
- <sup>24</sup> H. Monkhorst and J. Pack, Physical Review B **13**, 5188 (1976).
- <sup>25</sup> M. Methfessel and A. T. Paxton, Phys. Rev. B **40**, 3616 (1989).
- <sup>26</sup> P. H. T. Philipsen and E. J. Baerends, Phys. Rev. B **54**, 5326 (1996).
- <sup>27</sup> A. Devey and N. H. de Leeuw, Phys. Rev. B **82**, 235112 (2010).
- <sup>28</sup> J. H. Rose, J. R. Smith, F. Guinea, and J. Ferrante, Phys. Rev. B **29**, 2963 (1984).
- <sup>29</sup> M. T. Yin and M. L. Cohen, Phys. Rev. B **29**, 6996 (1984).
- <sup>30</sup> F. D. Murnaghan, Proceedings of the National Academy of Science **30**, 244 (1944).
- <sup>31</sup> F. Murnaghan, *Finite deformation of an elastic solid* (Dover New York, 1967).
- <sup>32</sup> C. S. Wang, B. M. Klein, and H. Krakauer, Phys. Rev. Lett. **54**, 1852 (1985).
- <sup>33</sup> J. Donohue, *The structures of the elements* (R.E. Krieger Pub. Co., Malabar, Fla., 1982) p. 256.
- <sup>34</sup> H. J. McSkimin, J. P. Andreatch, and P. Glynn, Journal of Applied Physics **43**, 985 (1972).
- <sup>35</sup> L. Brewer, LB-3720 (unpublished).
- <sup>36</sup> S. Fahy and S. G. Louie, Phys. Rev. B **36**, 3373 (1987).
- <sup>37</sup> O. L. Anderson, Journal of Physics and Chemistry of Solids **27**, 547 (1966).
- <sup>38</sup> M. Tschopp, K. Solanki, M. Baskes, F. Gao, X. Sun, and M. Horstemeyer, Journal of Nuclear Materials , (2011).
- <sup>39</sup> M. McKay, R. Beckman, and W. Conover, Technometrics **42**, 55 (2000).
- <sup>40</sup> C. Jiang, S. G. Srinivasan, a. Caro, and S. a. Maloy, Journal of Applied Physics **103**, 043502 (2008).
- <sup>41</sup> J. Häglund, G. Grimvall, and T. Jarlborg, Phys. Rev. B **44**, 2914 (1991).
- <sup>42</sup> M. Umemoto, Z. Liu, K. Masuyama, and K. Tsuchiya, Scripta Materialia **45**, 391 (2001).
- <sup>43</sup> K. Panda and K. R. Chandran, Acta Materialia **54**, 1641 (2006).
- <sup>44</sup> R. Hill, Proceedings of the Physical Society. Section A **65**, 349 (1952).
- <sup>45</sup> H. P. Scott, Q. Williams, and E. Knittle, Geophys. Res. Lett. **28**, 1875 (2001).
- <sup>46</sup> F. Laszlo and H. Nolle, Journal of the Mechanics and Physics of Solids **7**, 193 (1959).
- <sup>47</sup> H. Mizubayashi, S. Li, H. Yumoto, and M. Shimotomai, Scripta Materialia **40**, 773 (1999).
- <sup>48</sup> W. Chiou, Surface Science **530**, 87 (2003).
- <sup>49</sup> A. B. Belonoshko, Geochimica et Cosmochimica Acta **58**, 4039 (1994).
- <sup>50</sup> G. Naeser, Mitt. Kais.-Wilh.-Inst. Eisenforschg **16**, 207 (1934), as reported in Dick et al.<sup>52</sup>.
- <sup>51</sup> R. C. Reed and J. H. Root, Scripta Materialia **38**, 95 (1997).
- <sup>52</sup> A. Dick, F. Körmann, T. Hickel, and J. Neugebauer, Physical Review B **84**, 1 (2011).